2022

A Digital Twin for Synchronized Multi-Laser Powder Bed Fusion (M-LPBF) Additive Manufacturing

Shayna Petitjean
Wright State University

A DIGITAL TWIN FOR SYNCHRONIZED MULTI-LASER POWDER BED FUSION (M-LPBF) ADDITIVE MANUFACTURING

A thesis submitted in partial fulfillment of the
requirements for the degree of
Master of Science in Mechanical Engineering

By

SHAYNA PETITJEAN
B.S.M.E., Wright State University, 2020

2022
Wright State University

WRIGHT STATE UNIVERSITY

GRADUATE SCHOOL

April 28, 2022

I HEREBY RECOMMEND THAT THE THESIS PREPARED UNDER MY SUPERVISION BY Shayna Petitjean ENTITLED A Digital Twin for Synchronized Multi-Laser Powder Bed Fusion (M-LPBF) Additive Manufacturing BE ACCEPTED IN PARTIAL FULFILLMENT OF THE REQUIREMENTS FOR THE DEGREE OF Master of Science in Mechanical Engineering.

_____

Hamed Attariani, Ph.D.
Thesis Director

_____

Raghavan Srinivasan, Ph.D., P.E.
Chair, Department of Mechanical Engineering

Committee on Final Examination:

_____

Nathan W. Klingbeil, Ph.D.

_____

Ahsan Mian, Ph.D.

_____

Barry Milligan, Ph.D.
Vice Provost for Academic Affairs
Dean of the Graduate School

Abstract

Petitjean, Shayna. MSME Department of Mechanical and Materials Engineering, Wright State University, 2022. A Digital Twin for Synchronized Multi-Laser Powder Bed Fusion (M-LPBF) Additive Manufacturing.

One of the technological challenges in the widespread application of additive manufacturing is the formation of undesired material microstructure and defects. Specifically, in metal additive manufacturing, the microstructural formation of columnar grains in Ti-6Al-4V is common and results in anisotropic mechanical properties and a reduction in properties such as ductility and endurance limit. This work presents the application of hexagonal and circular arrays of synchronized lasers to alter the microstructure of Ti-6Al-4V in favor of equiaxed grains. An anisotropic heat transfer model obtains the temporal/spatial temperature distribution and constructs the solidification map for various process parameters, including laser power, laser scanning speed, and internal distance between lasers in the array. Some degree of laser overlap is recommended to maintain continuous melt pools. The results, particularly at higher power settings and lower scanning speeds, indicate the attainability of equiaxed grains, suggesting a degree of control in microstructure formation in additive manufacturing.

Contents

Table of Figures

List of Tables

Acknowledgments

Firstly, I would like to express my sincerest gratitude to Dr. Hamed Attariani for all the knowledge, opportunity, and patience he has afforded me. Without his continued support, none of this would have been possible for me.

I would also like to thank Dr. Ahsan Mian and Dr. Nathan W. Klingbeil for putting forth the time and energy to consider my work as members of my committee.

Finally, I wish to express the biggest of thanks to my husband, Adam. Always.

For Mom

1. Introduction

Laser additive manufacturing (LAM) allows for the fabrication of complex three-dimensional parts comprised of various materials, including metals and ceramics [1,2]. However, the mechanical properties of the final product of LAM are unpredictable and lead to overall quality uncertainties. This unpredictability in mechanical properties stems from formation defects such as residual porosity, spatter, lack of fusion, cracks, surface roughness, and undesired microstructure [2,3]. For example, surface roughness and lack of fusion pores lead to poor fatigue [3]. In addition, the LAM of Ti-6Al-4V leads to the formation of long columnar grains that align with the laser scanning direction [4], resulting in a reduction in endurance limit and anisotropic properties [5].

Many studies have been conducted to better understand how LAM can be utilized to control resulting mechanical properties to improve the widespread application of additive manufacturing. This work seeks to further these studies, specifically regarding laser powder bed fusion (LPBF) and material microstructure control. LPBF is a branch of LAM that consists of selectively melting and solidifying powdered material layer by layer until the desired product is complete. This method is often used to process metals such as Ti-6Al-4V. Ti-6Al-4V meets two critical criteria that allow it to be additively manufactured: good weldability to avoid cracks during solidification and its availability as small, spherical powders that allow good packing density and homogeneity [6]. It has been found that the LAM of Ti-6Al-4V tends to result in long columnar grains in all but high laser power applications [4]. It has also been shown that a correlation exists between laser scanning speed and the scale of columnar grains- as laser scan decreases, the scale of columnar grains increases [4].

An additively manufactured material's microstructure is driven by its cooling (solidification rate) and thermal gradient. Rapid solidification rates and large thermal gradients result in columnar-dominated microstructures [6]. Finding a way to modify these parameters could create an opportunity to control microstructure and, therefore, mechanical properties. However, accomplishing this via conventional, single-laser methods has not shown much promise in practicality. This work investigates the application of multi-beam laser configurations for LPBF and its effect on the microstructure. However, few studies have investigated the effect of multi-laser-based additive manufacturing on microstructure. Evans et al. sought to understand the effect of two coordinated laser beams on microstructure in LPBF via a Rosenthal solution and a semi-analytical approach [7]. While it was found that melt pool shape and size could be altered, microstructure could not. Dezfoil et al. implemented a dual-laser configuration in a study that resulted in a more uniform microstructure that remained columnar [8]. Heeling et al. implemented a similar configuration and showed that adding a second laser beam near the melt pool resulted in briefly suspending the solidification rate of the material [9], thus increasing the probability of a more desirable microstructure.

In a work considering a configuration of five laser beams, an analytical solution was utilized to study the effect of laser configuration on material microstructure [10]. While the results indicate success in achieving a high average probability of equiaxed grain growth by laser position control, the model used was simplified and lacked validation. In another study by Heeling et al., a comprehensive computational model was developed for two synchronized lasers that incorporated the temperature dependency of material properties, Marangoni effects, convection, and radiation [11]. It is worth noting that analytical methods, such as the Rosenthal equation, assume thermos-physical properties such as thermal conductivity, density, and specific heat, are independent of

temperature and neglect heat transfer due to radiation and convection [12]. The model developed for this work considers the temperature dependency of these properties, while other multi-beam laser studies focus of many strays from microstructure control and find greater interest in residual stress reduction [13-17] and fabrication time reduction [18].

This work features the exploration of two synchronized multi-laser beam configurations to discover the feasibility of controlling the material microstructure of Ti-6Al-4V in LPBF. A computational model is developed and used to predict the melt pool dimensions of width and depth for a single laser scanning at a constant speed for a range of speeds. These results are compared to those found experimentally. Upon validation, the model is utilized to simulate two laser configurations: 1) seven lasers arranged in a hexagonal configuration and 2) five lasers in a circular array. Three constant power settings are considered at three constant laser scanning speeds, each at five different laser spacings. Melt pool dimensions and thermal gradients are collected for each of these simulations. The thermal gradients are then used to determine the solidification rates. These two parameters are used to construct solidification maps, and the resulting microstructure is determined utilizing Hunt's criterion.

2. Computational Model

Multiphysics Object-Oriented Simulation Environment (MOOSE) software is used to solve the heat conduction equation and predict melt pool dimensions. The dimensions representing the powder bed are $1\times1\times0.5$ mm^3 for the model-verifying single laser simulations, while those representing the power bed are $5\times1.5\times1.5$ mm^3 for the multi-laser configurations. Eight-node hexahedral elements with dimensions of $10\times10\times7.5$ μm^3 are utilized to mesh the simulation domain. It should be noted that the powder diameter is typically around 30-50 μm. A finer mesh

of 5×5×5 μm^3 is utilized to check the effect of the mesh size on the results, and it is found that the melt pool dimensions only changed by 0.1%. Therefore, to reduce the computational time and the financial cost of each simulation, the less fine 10×10×7.5 μm^3 mesh is used. The size of the simulation domain is adequate for transient thermal analysis since it is at least ten times larger than thermal diffusion length based on the laser velocity range, $l_{th} = \sqrt{Dr_0/v}$=0.036-0.025 mm [19], where v is scanning velocity, D is thermal diffusivity, and r_0 is laser beam radius. The laser power and scanning speed range are selected to ensure that the melting occurs dominantly in the *conduction* regime [20] (see Figure 20 in the Appendix). In LAM, the melt pool created by a laser heat source can be either in 'conduction' or 'keyhole' mode [8]. Heat is primarily transferred via conduction in conduction mode melting and convection in keyhole mode melting. The melt pool tends to be shallow and wide in conduction mode, whereas in keyhole mode, it tends to be deep and narrow [20]. The conduction mode is generally favored due to better control of heat input, higher process stability, and higher quality (i.e., fewer defects). Model parameters can be found in Table 1.

Table 1. Model parameters for LPBF-AM of Ti-6Al-4V [21].

Parameter	**Notation**	**Unit**	**Value**
Solidus Temperature	T_S	K	1878
Melting Temperature	T_m	K	1923
Liquidus Temperature	T_L	K	1993
Absorption Coefficient	A	-	0.25
Laser Beam Radius	r_o	μm	75
Laser Power	P	W	50, 300, 500, 1000
Laser Scanning Speed	v	mm/s	100 - 1000
Melting Enthalpy	H_f	kJ/kg	370
Thermal Conductivity Enhancement Factors	λ_x, λ_y, λ_z	-	10, 10, 15
Heat Transfer Convection	h_c	W/m^{2}K	50
Heat Transfer Radiation	h_f	W/m^{2}K	1

2.1. Governing Equations

The transient temperature distribution is obtained by using the anisotropic thermal conductivity model

$$c_p\rho\frac{\partial T}{\partial t} = \frac{\partial}{\partial x}\left(\lambda_x k_x \frac{\partial T}{\partial x}\right) + \frac{\partial}{\partial y}\left(\lambda_y k_y \frac{\partial T}{\partial y}\right) + \frac{\partial}{\partial z}\left(\lambda_z k_z \frac{\partial T}{\partial z}\right) - \rho H_f \frac{\partial \alpha}{\partial t} \quad (1)$$

where c_p is the specific heat capacity, ρ is the density, λ_n is the thermal conductivity enhancement factors, k_n is the thermal conductivity, H_f is the melting enthalpy, α is the melt fraction ($\alpha = 1$ indicates liquidus phase, and $\alpha = 0$ indicates solidus phase), T is the powder bed temperature, and t represents time. The melt fraction parameter can be further defined as

$$\alpha = \begin{cases} 0, & T < T_S \\ (T - T_S)/(T_L - T_S), & T_S < T < T_L \\ 1, & T > T_L \end{cases} \quad (2)$$

where T_S is the solidus temperature, and T_L is the liquidus temperature. This simplified model mimics the effect of Marangoni convection in the melt pool and considers heat absorption during melting. The Gaussian heat flux was used to model a moving laser heating the top surface

$$q(x,y) = \frac{2PA}{\pi r_o^2}\exp\left(-\frac{2((x-vt)^2 - y^2}{r_o^2}\right) \quad (3)$$

where A is the laser absorption coefficient, and v, P, and r_0 are the laser scanning speed, power, and spot radius, respectively. Convection and radiation boundary conditions were added to all surfaces except the bottom of the powder bed.

$$\dot{q} = h_c(T - T_0) + h_r(T^4 - T_0^4) \quad (4)$$

$$\dot{q} = q(x,y) + h_c(T - T_0) + h_r(T^4 - T_0^4) \quad (5)$$

where h_c and h_r are the convective and radiation heat transfer coefficients, respectively, and T_0 is room temperature. The symmetric boundary condition was applied to reduce the computational

cost. All model parameters are summarized in Table 1, and the Ti-6Al-4V alloy's thermo-physical properties are included in Table 2, located in the Appendix.

2.2. Model Verification

Before applying the model to multi-beam laser arrays, it was applied in the case of a single laser beam. The resulting melt pool dimensions of width and depth were compared to experimental results obtained by Yin et al. [22] using a laser power of 300 W and parameters defined in Table 1. The simulations were conducted for laser scanning speeds of 500, 600, 700, 800, 900, and 1000 mm/s. The melt pool dimensions predicted by the model and the experimental dimensions by Yin et al. can be found in Figure 1.

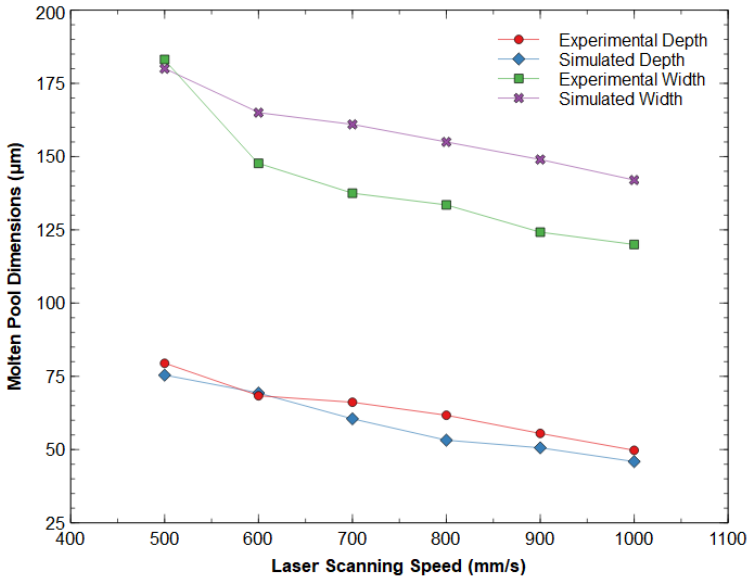

Figure 1. Simulated melt pool dimensions vs. experimental melt pool dimensions for laser scanning speeds 500-1000 mm/s.

Overall, the model results agree with the experimental results. The greatest error percentage occurs in the comparison of width and increases with scanning speed from about 1.72% at 500 mm/s to about 19.96% at 1000 mm/s. The error percentage in the comparison of depth ranges from about

1.37% to about 13.80%. All simulation results and experimental comparisons can be found in Tables 3 and 4, respectively, in the Appendix.

To reduce computational modeling expenses, the dependency of anisotropic thermal conductivity with laser power and scanning speed [23] is neglected. Furthermore, uncertainties in modeling and physical parameters, including potential temperature dependence of the laser absorption coefficient [24], various mathematical models for laser-beam heat sources [25,26], and temperature dependence of density and thermal conductivity with powder porosity [27], should be noted.

In addition, the resulting overall shape of the melt pool agrees with what is expected, including a comet-like long tail [28]. The shape of the melt pool is shown in Figure 2.

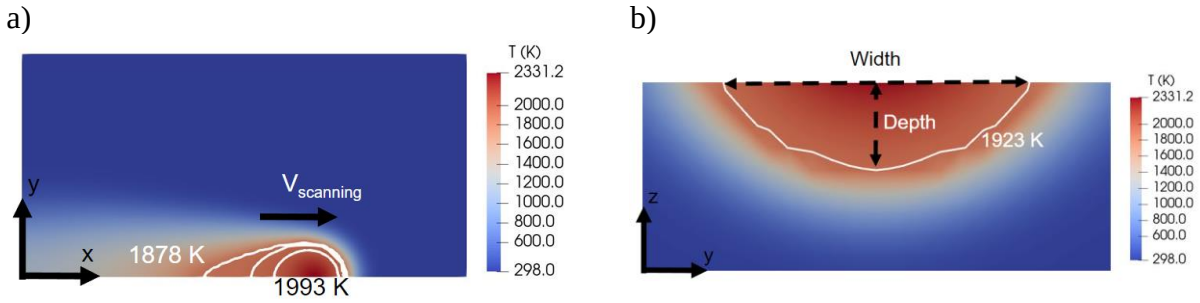

Figure 2. The melt pool shape for a single laser beam. a) The shape from the scanning direction with a solidus (1878 K) and liquidus (1993 K) contours. b) Temperature distribution and definition of depth and width of the melt pool based on melting temperature (1923 K).

2.3. Solidification Map

The thermal gradient $|\vec{G}|$ and solidification rate (R) are calculated to construct the solidification map as

$$|\vec{G}| = \sqrt{\left(\frac{\partial T}{\partial x}\right)^2 + \left(\frac{\partial T}{\partial y}\right)^2 + \left(\frac{\partial T}{\partial z}\right)^2} \quad (6)$$

and

$$R = v\frac{G_x}{|G|} \tag{7}$$

where

$$G_x = \frac{\partial T}{\partial x} \tag{8}$$

The resulting solidification map for the model-verifying single-laser simulation can be found in Figure 3a. *R* is calculated for the cooling zone of the melt pool where *R* is greater than zero. *R* is less than zero in the heating zone and does not factor in the determination of microstructure. Figure 3b shows liquidus surface contours for *R* and $|\vec{G}|$ in the cooling zone of the melt pool. There is significant variation of *R* and $|\vec{G}|$ along the liquidus surface, and it is shown that the thermal gradient at the bottom of the melt pool is much greater than that at the top. This indicates that as melt pool depth increases, thermal gradient and the likelihood of columnar grain increases [12]. It is also shown in Figure 3b that the solidification rate also varies along the liquidus surface. It is near zero at the bottom of the melt pool, where the heating zone transitions into the cooling zone and increases as the contour reaches the tail of the melt pool. Mixed and equiaxed grains are more likely to form at the tail of the melt pool. From Figure 3a, it is shown that the single-laser simulations conformed to expectations. A columnar microstructure is predicted for the bottom of each melting pool, as indicated by point 'B'. A mixed microstructure is predicted for the tail of each melting pool, as indicated by point 'S'. Furthermore, it is shown that as laser scanning speed increases, *R* x *G* increases. This indicates a decrease in grain size and agrees with previous studies [29,30].

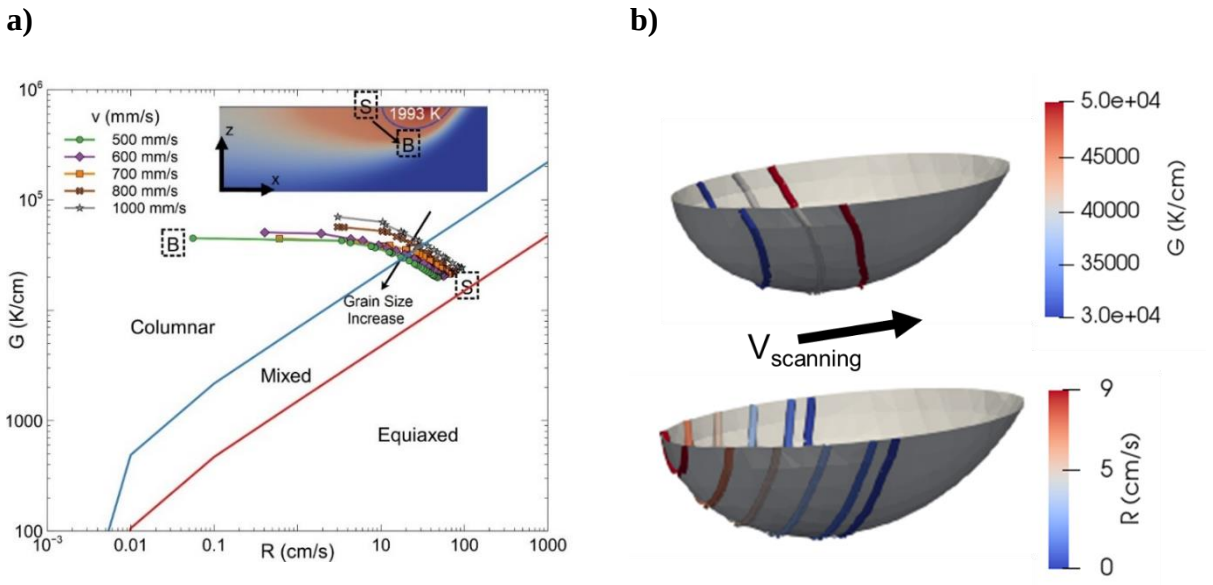

Figure 3. a) Solidification map for simulated single laser results and b) melt pool contour.

The results of the single-laser simulations are encouraging. As such, the model used is modified to accommodate hexagonal and circular configurations in the following two sections.

3. Multi-beam Laser Powder Bed Fusion

This study modeled two possible laser configurations, i.e., hexagonal and circular laser arrays. The hexagonal laser configuration consists of seven synchronized lasers, and the circular array includes five lasers. It is worth noting that the distance between lasers in the array is constant during the scanning process.

3.1. Hexagonal Configuration

Upon model validation, a multi-laser hexagonal configuration was considered. A two-dimensional representation of the configuration is shown in Figure 4.

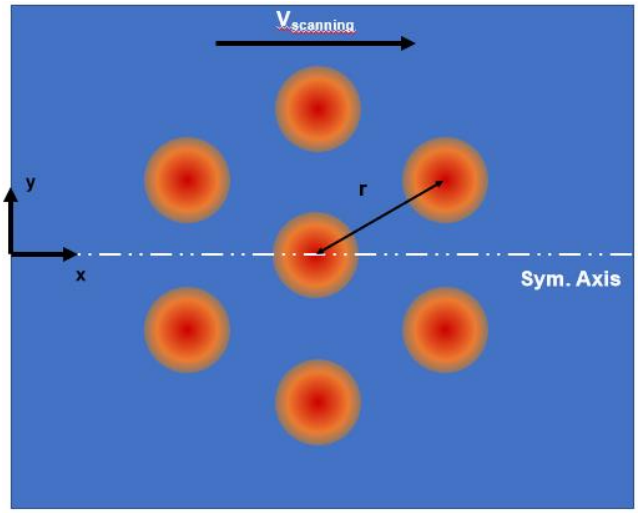

Figure 4. Two-dimensional visual representation of the hexagonal configuration.

Figure 5 provides the three-dimensional visualizations of the lasers' heat flux in Gaussian distribution when the internal distance between lasers is a) 50 µm and b) 250 µm

a) **b)**

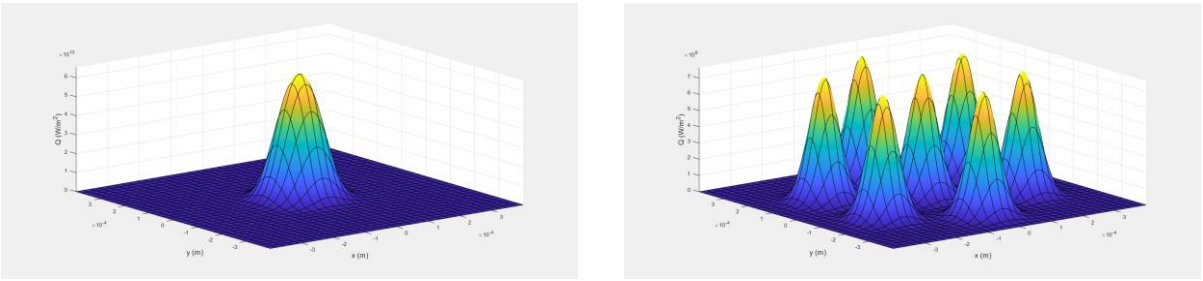

Figure 5. Gaussian distribution for hexagonal configurations with r of a) 50 µm and b) 250 µm.

Three power settings (50, 300, and 500 W) are considered for the hexagonal configuration simulations. In each simulation, all lasers are set to the same power setting, *P*. Three laser scanning speeds (100, 500, and 1000 mm/s) are considered for each *P*, and five distances between laser beams (50, 75, 150, 200, and 250 µm) were considered for each laser scanning speed, *v*.

3.1.1. Melt Pool and Solidification Map

For each simulation, resulting melt pool dimensions of width and depth are captured and plotted to compare the effect of the internal distance between lasers, *r*, on melt pool shape for each *v* for each *P*. For example, Figure 6 displays the melt pool shapes for a *P* of 500 W at *v* of 100-1000 mm/s for *r* of 50-250 µm. In each melt pool shape plot, the x-axis represents the laser scanning speed direction, the y-axis represents the width, and the *z* corresponds to depth. From Figure 6, it is shown that melt pool depth and width both tend to decrease as *v* increases. This is likely due to the decreased interaction time between the lasers and the powder bed material. A decrease in interaction time between the two results in a reduction in heat absorption and thermal crosstalk. Figure 6 also shows that as *r* increases, width tends to increase. For example, at an *r* of 50 µm for a *v* of 500 mm/s, the width is found to be 532 µm, whereas, at an *r* of 250 µm, the width is found to be 720 µm. This can be justified given that a greater *r*-value indicates a more spread-out configuration (i.e., the configuration covers more surface area). Also, as *r* increases, depth tends to decrease overall. For the same *v*, at an *r* of 50 µm, the depth is found to be 308 µm, whereas, at an *r* of 250 µm, the depth is found to be 230 µm.

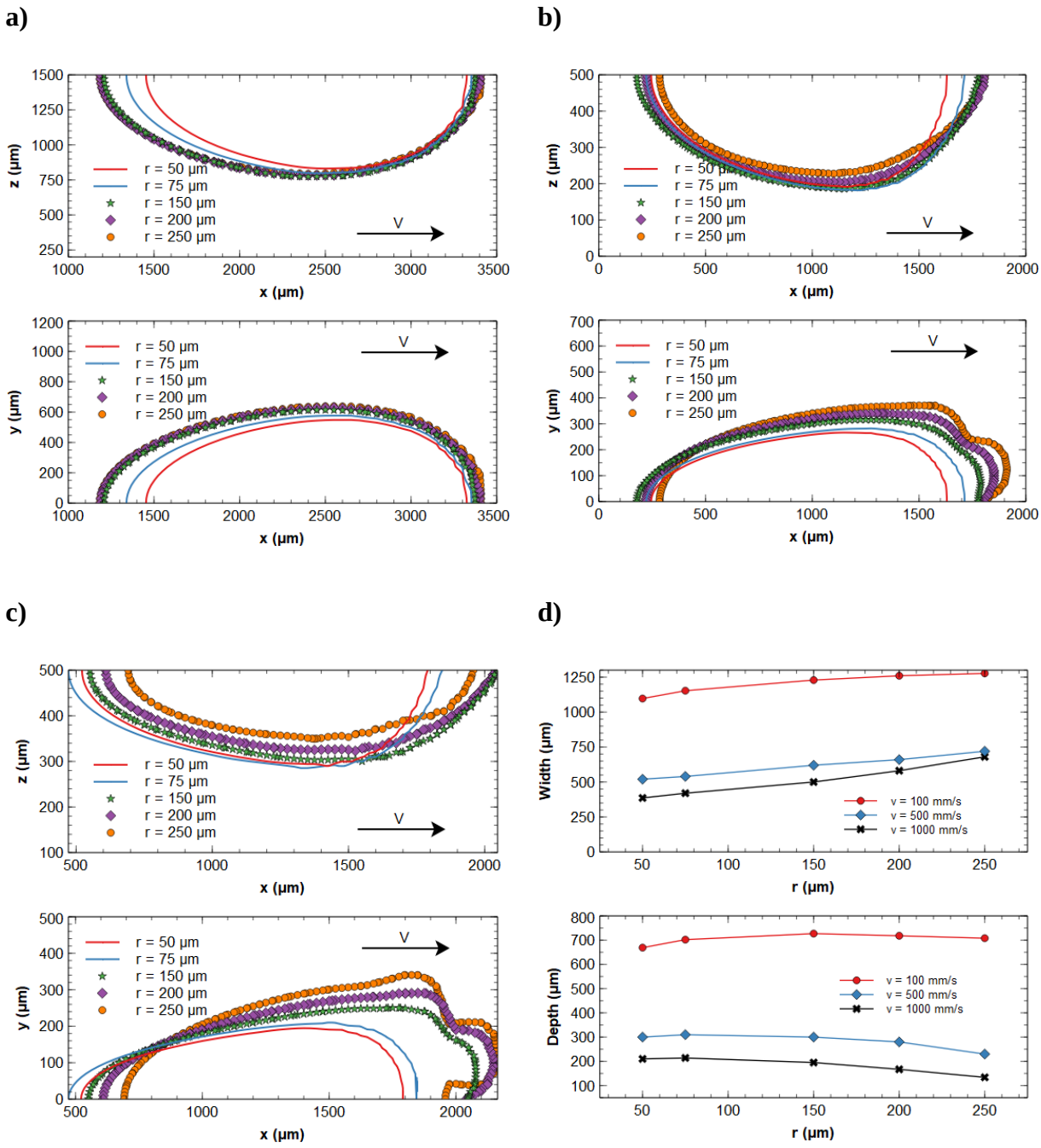

Figure 6. Melt pool shapes for P = 500 W at a) 100 mm/s, b) 500 mm/s, and c) 1000 mm/s and d) melt pool dimensions in hexagonal configuration.

Scaling the power setting back to 50 W, the melt pool shapes seem to mimic those at 500 W; however, beginning at an *r* of 200 µm for a *v* of 100 mm/s and at an *r* of 150 µm for the higher speeds, the melt pool appears to separate into multiple melt pools. This is shown in Figure 7. The overall trends remain the same for the continuous melt pools- as *r* increases, melt pool width increases while depth decreases.

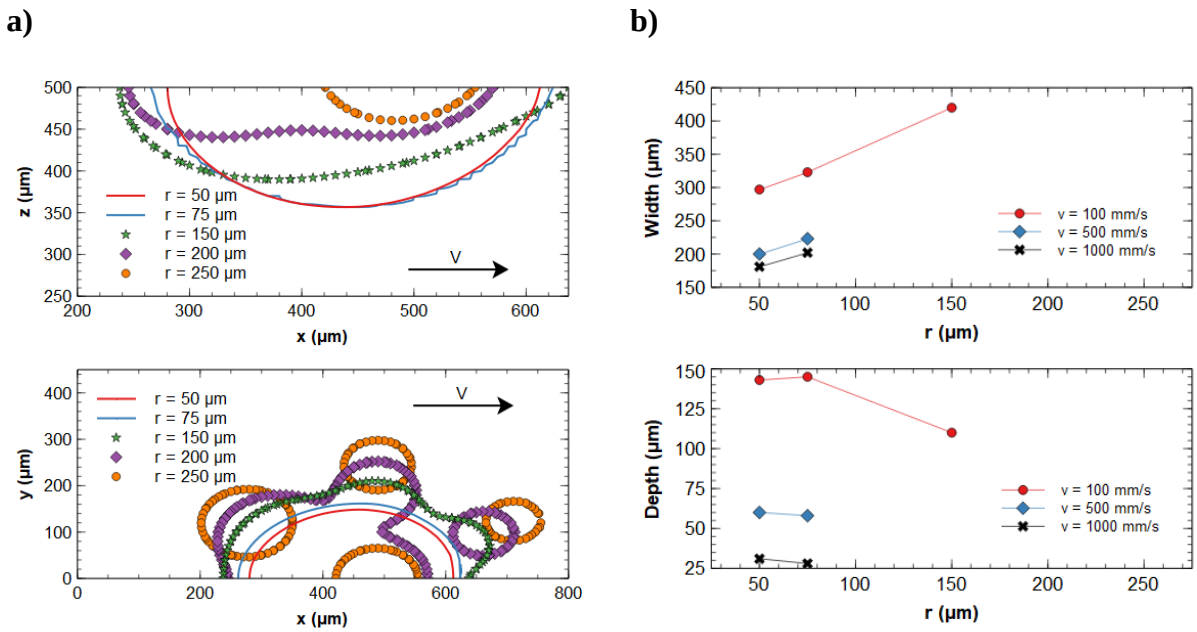

Figure 7. a) Melt pool shape and b) melt pool dimensions for P = 50 W at 100 mm/s.

Melt pool shapes and dimensions for *P* of 300 W in hexagonal configuration corroborate these trends and can be found in Figure 21 located in the Appendix.

The solidification map for all hexagonal configuration simulations for a *P* of 50 W at *v* of 100-1000 mm/s for *r* of 50-250 µm is displayed in Figure 8.

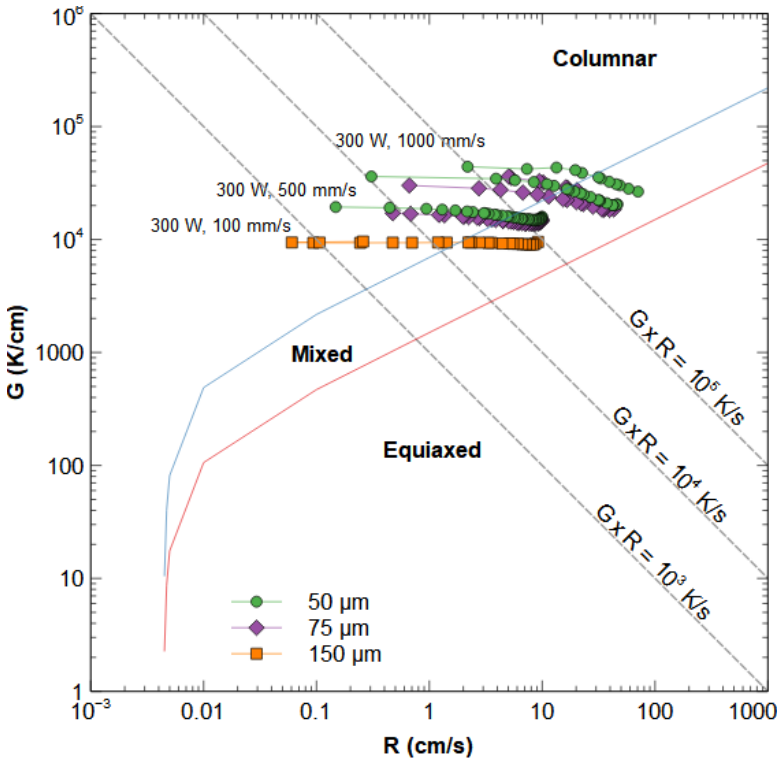

Figure 8. Solidification map for hexagonal configurations at P = 50 W.

From Figure 8, it can be discerned that an equiaxed microstructure is not attained at a power setting of 50 W. All microstructures are expected to be either mixed or columnar. It is also shown that as laser scanning speed increases, *G* x *R* values increase. This indicates a decrease in grain size as laser scanning speed increases.

In comparison, Figure 9 displays the solidification maps for a *P* of (a) 300 W and (b) 500 W at *v* of 100-1000 mm/s for *r* of 50-250 µm.

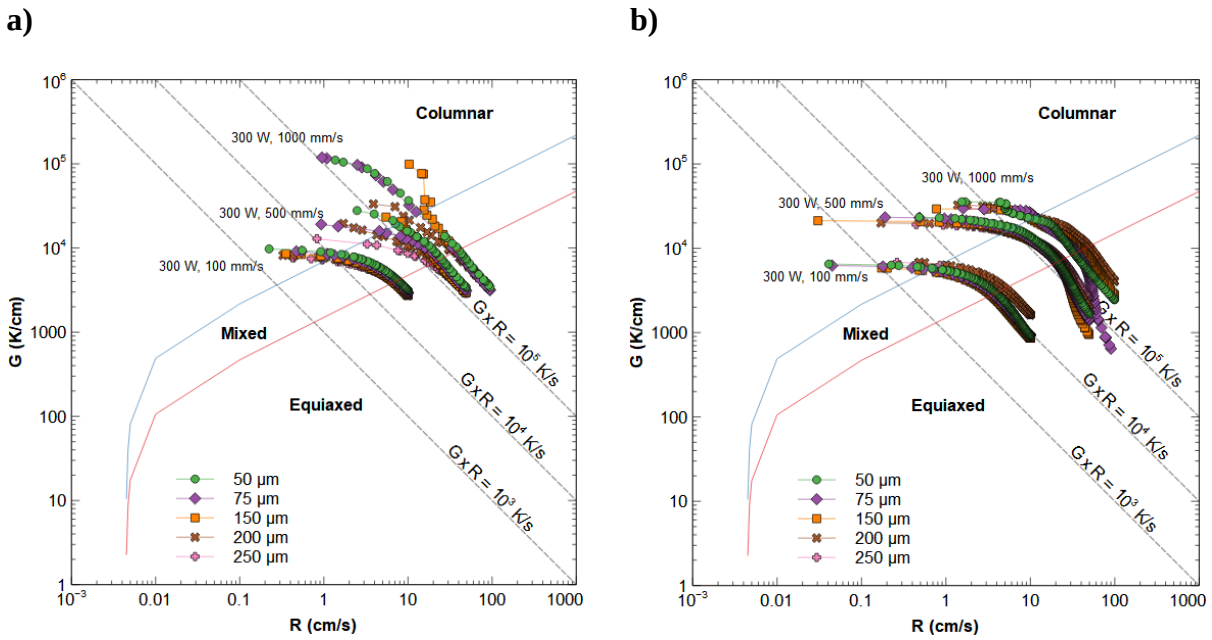

Figure 9. Solidification maps for hexagonal configurations at P = a) 300 W and b) 500 W.

At 300 and 500 W, an equiaxed microstructure is attained. Referring to Figure 3a, these equiaxed grains will form at the tail of the melt pool (point S) and extend to its depth. From the deepest point of the melt pool (point B), columnar grains will emerge to meet the equiaxed to form the mixed region. Grain size continues to decrease with increasing laser scanning speed.

3.1.2. Predicted Microstructure by Volume Fraction

From the thermal gradient, solidification rate, and melt pool arc length, it is possible to roughly approximate the volume fraction of equiaxed, mixed, and columnar microstructure for each simulation. Using the Hunt's criteria

$$\frac{G^{1.91}}{R} < 1.04 \times 10^{6} \frac{K^{1.91}}{cm^{2.91} \cdot s} \text{ for equiaxed microstructure} \quad (9)$$

and

$$\frac{G^{1.91}}{R} > 1.92 \times 10^{6} \frac{K^{1.91}}{cm^{2.91} \cdot s} \text{ for columnar microstructure,} \quad (10)$$

The melt pool's equiaxed, mixed, and columnar portions could be discerned. The x- and y-coordinates corresponding to values of *G* and *R* utilized in the criteria of Eqs. (9) and (10) for *P* of 500 W, *v* of 100 mm/s, and *r* of 50 µm are plotted in Figure 10.

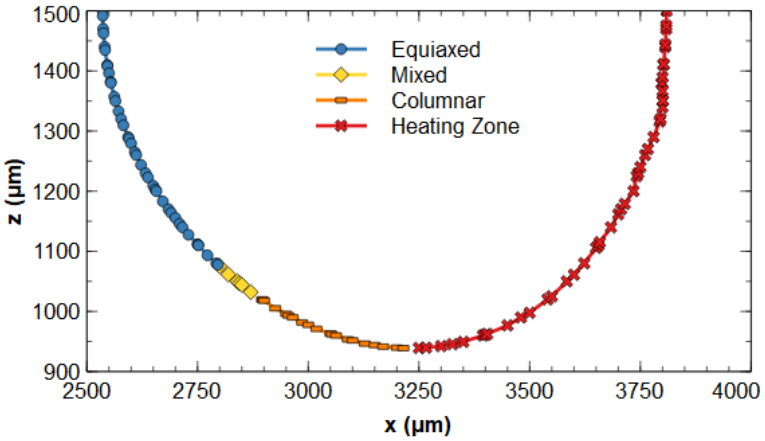

Figure 10. Predicted microstructure of melt pool depth for P = 50 W, v = 100 mm/s, and r = 50 µm.

Using the concept of arc length from the x- and z-coordinates, the volume fractions of each microstructure are found. The 300 and 500-W power settings results can be found in Figures 11 and 12, respectively.

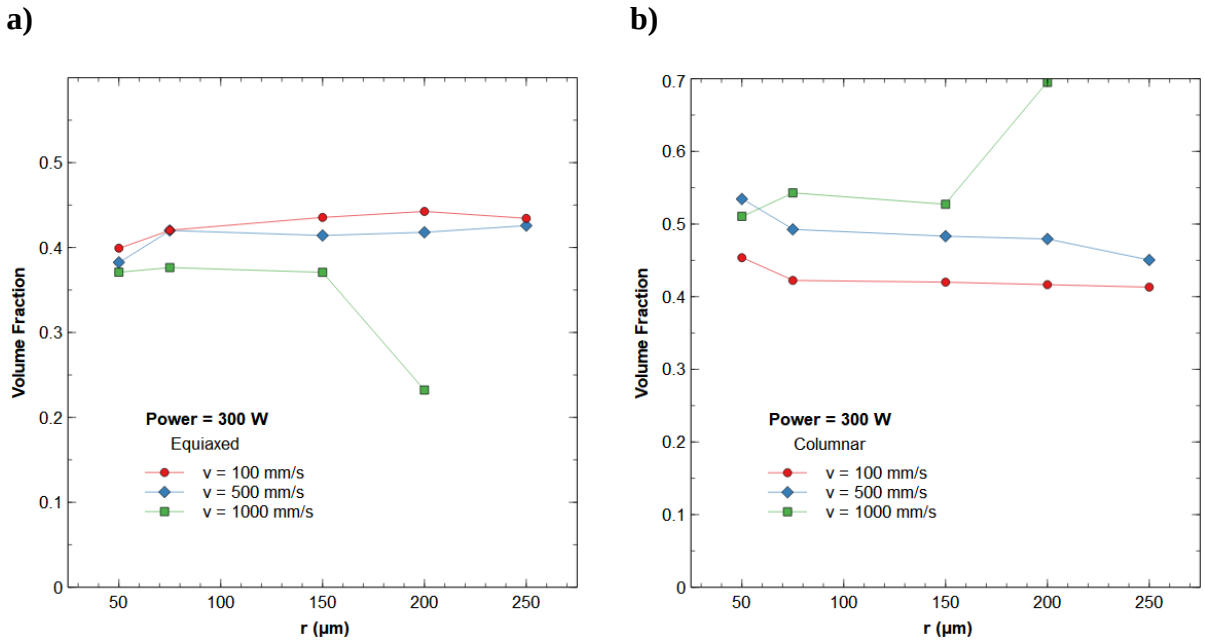

Figure 11. The volume fraction of a) equiaxed and b) columnar microstructures for hexagonal configurations at P = 300 W.

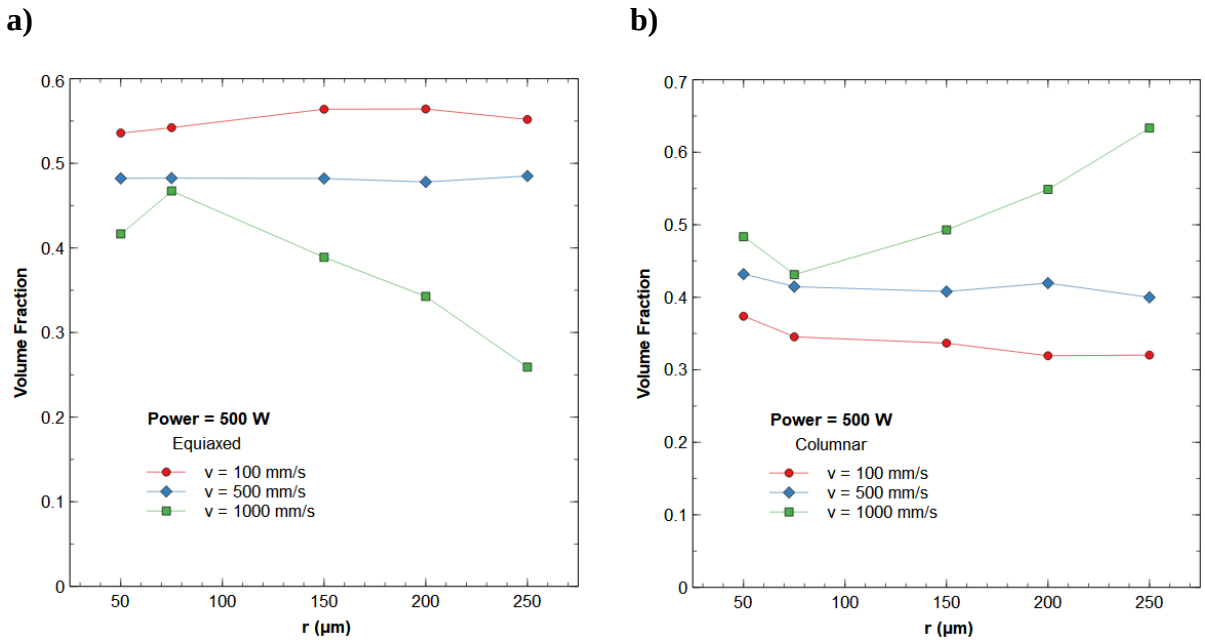

Figure 12. The volume fraction of a) equiaxed and b) columnar microstructures for hexagonal configurations at P = 500 W.

Figures 11a and 12a show that the volume fraction of equiaxed grains decreases as laser scanning speed increases. For a *P* of 300 W at 100 mm/s, the average percentage of equiaxed microstructure is about 43%, whereas, at 1000 mm/s, the average percentage of equiaxed microstructure is about 37%. It is also apparent that an increase in laser power results in an increase in the volume fraction of equiaxed grains. The resulting average percentage of equiaxed microstructure for a *P* of 300 W at 100 mm/s is about 43%, whereas the resulting average percentage of equiaxed microstructure for a *P* of 500 W at 100 mm/s is about 55%. In contrast, the volume fraction of columnar microstructure increases as laser scanning speed increases and decreases as laser power increases.

3.2. Circular Configuration

A circular configuration is considered next. A two-dimensional representation of the configuration is shown in Figure 13.

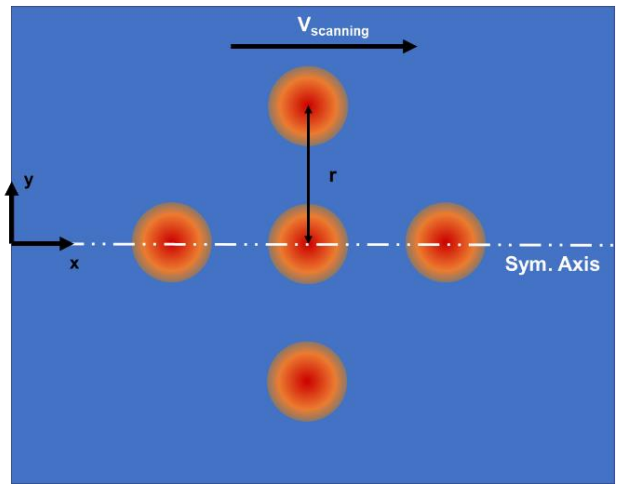

Figure 13. Two-dimensional visual representation of the circular configuration.

Figure 14 provides the three-dimensional visualizations of the lasers' heat flux in Gaussian distribution when *r* is (a) 50 µm and (b) 250 µm.

a) **b)**

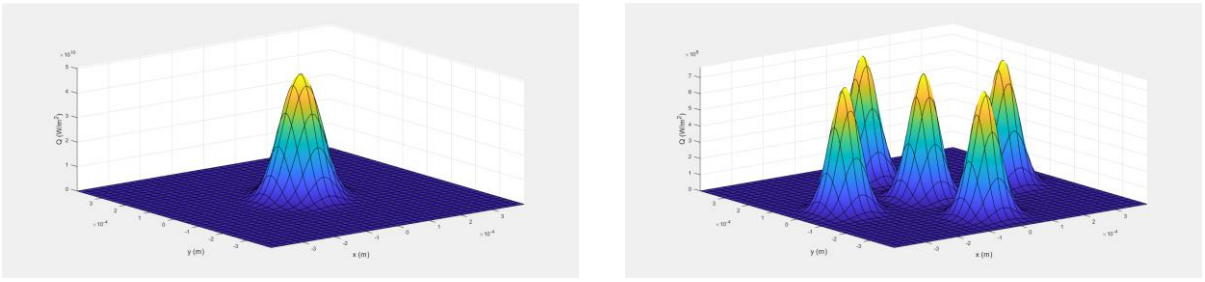

Figure 14. Gaussian distribution for circular configurations with r of a) 50 µm and b) 250 µm.

As with the hexagonal configuration simulations, three power settings (50, 300, and 500 W) are considered for the circular configuration simulations. In each simulation, all lasers are set to the same power setting, *P*. Three laser scanning speeds (100, 500, and 1000 mm/s) are considered for each *P*, and five distances between laser beams (50, 75, 150, 200, and 250 µm) are considered for each laser scanning speed, *v*.

3.2.1. Melt Pool and Solidification Map

Once again, the resulting melt pool dimensions of width and depth are captured and plotted to compare the effect *r* on melt pool shape for each *v* for each *P*. Figure 15 displays the melt pool shapes for a *P* of 500 W at *v* of 100-1000 mm/s for *r* of 50-250 µm.

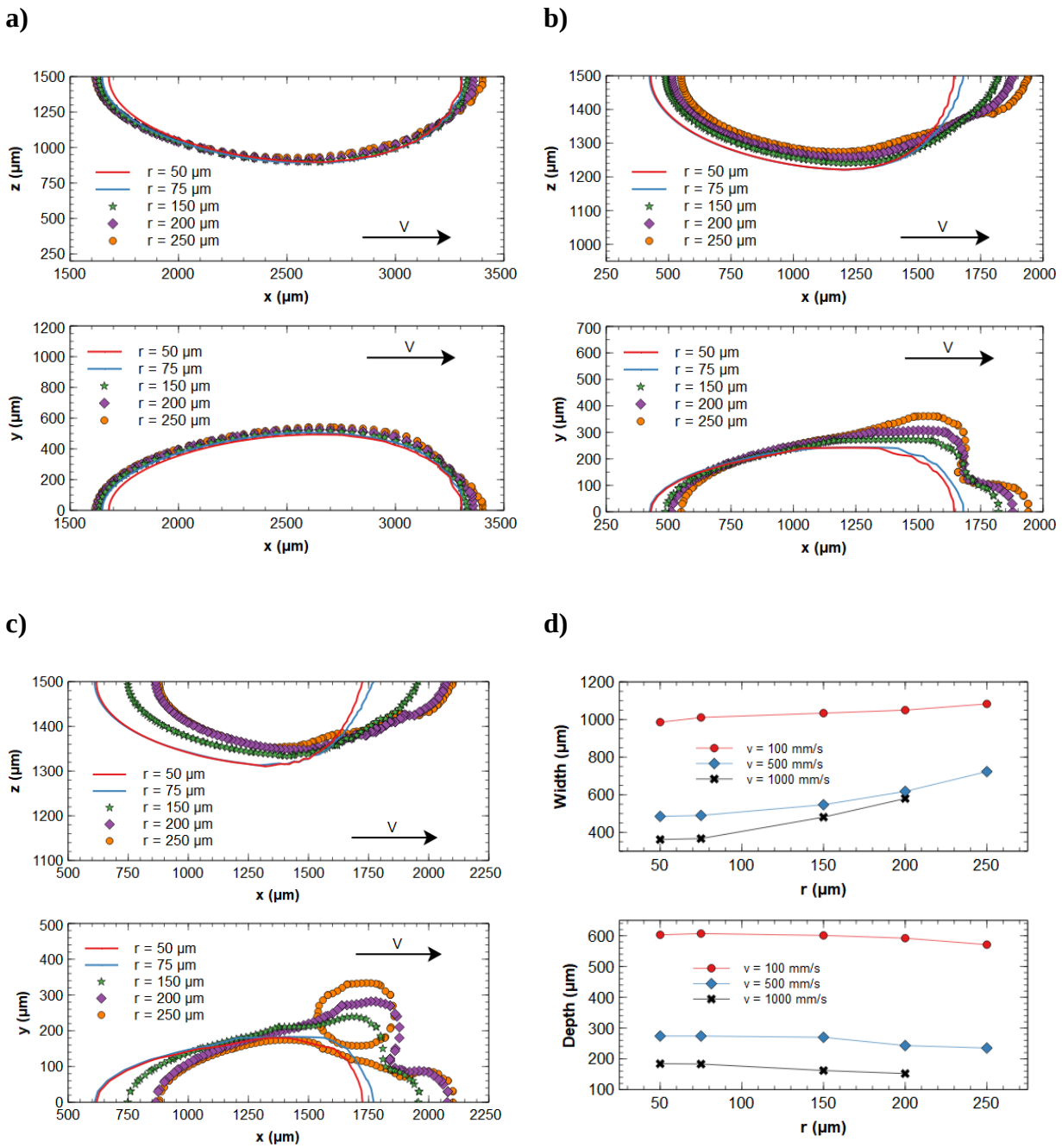

Figure 15. Melt pool shapes for P = 500 W at a) 100 mm/s, b) 500 mm/s, and c) 1000 mm/s in circular configuration. d) melt pool dimensions in circular configuration.

Aligning in trend with the resulting melt pool dimensions of the hexagonal configurations, the melt pool dimensions tend to decrease as laser scanning speed increases. Width is still shown to increase with increasing *r*, while depth is still shown to decrease with increasing *r*. Melt pool shapes and dimensions for *P* of 50 and 300 W in circular configuration further support these trends and are found in Figures 23 and 24, respectively, in the Appendix.

The solidification map for all circular configuration simulations for a *P* of 50 W at *v* of 100-1000 mm/s for *r* of 50-250 µm is displayed in Figure 16.

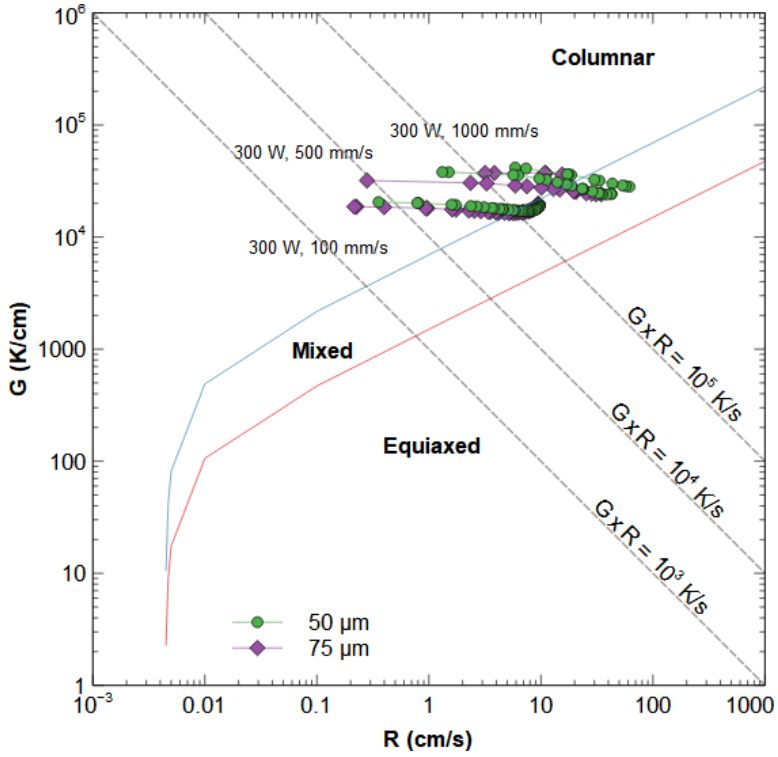

Figure 16. Solidification map for circular configurations at P = 50 W.

As in the hexagonal configuration simulations, all circular configuration simulations result in columnar and mixed microstructures. Equiaxed grains were not attained under any set conditions for this power setting. Furthermore, comparing the results in Figure 16 to those in Figure 8, the

circular configuration results in an overall decrease in grain size compared to those of the hexagonal configuration.

Figure 17 displays the solidification maps for a *P* of (a) 300 W and (b) 500 W at *v* of 100-1000 mm/s for *r* of 50-250 µm.

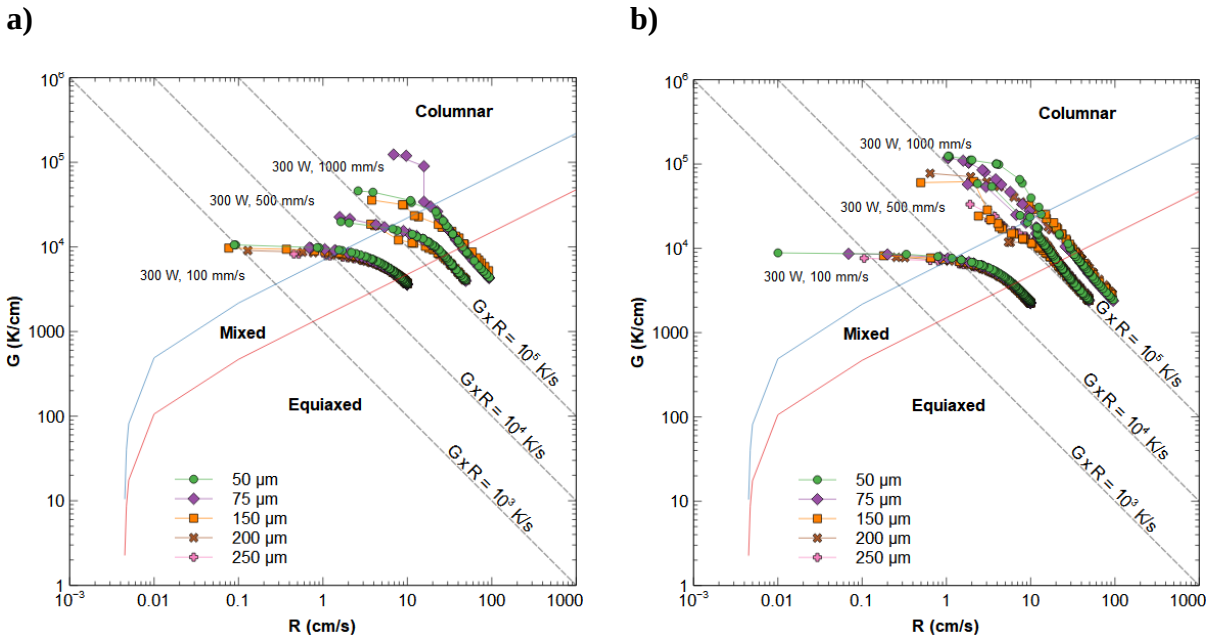

Figure 17. Solidification maps for circular configurations at P = a) 300 W and b) 500 W.

As with the hexagonal configuration, equiaxed grains begin to emerge for *P* of 300, and 500 W. Grain size decreases with increasing laser scanning, showing consistency with the results of the hexagonal simulations.

3.2.3. Predicted Microstructure by Volume Fraction

The volume fractions of equiaxed and columnar microstructure for each circular simulation are determined via the same procedure as described in section 3.1.2. The 300 and 500-W power settings results can be found in Figures 18 and 19.

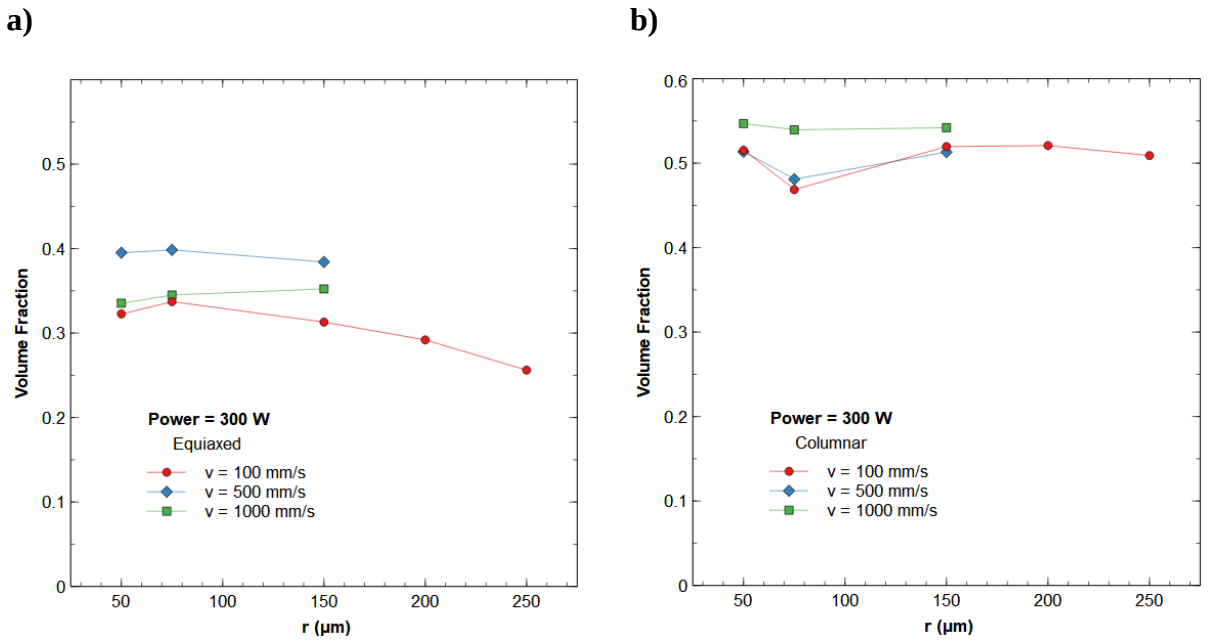

Figure 18. The volume fraction of a) equiaxed and b) columnar microstructures for circular configurations at P = 300 W.

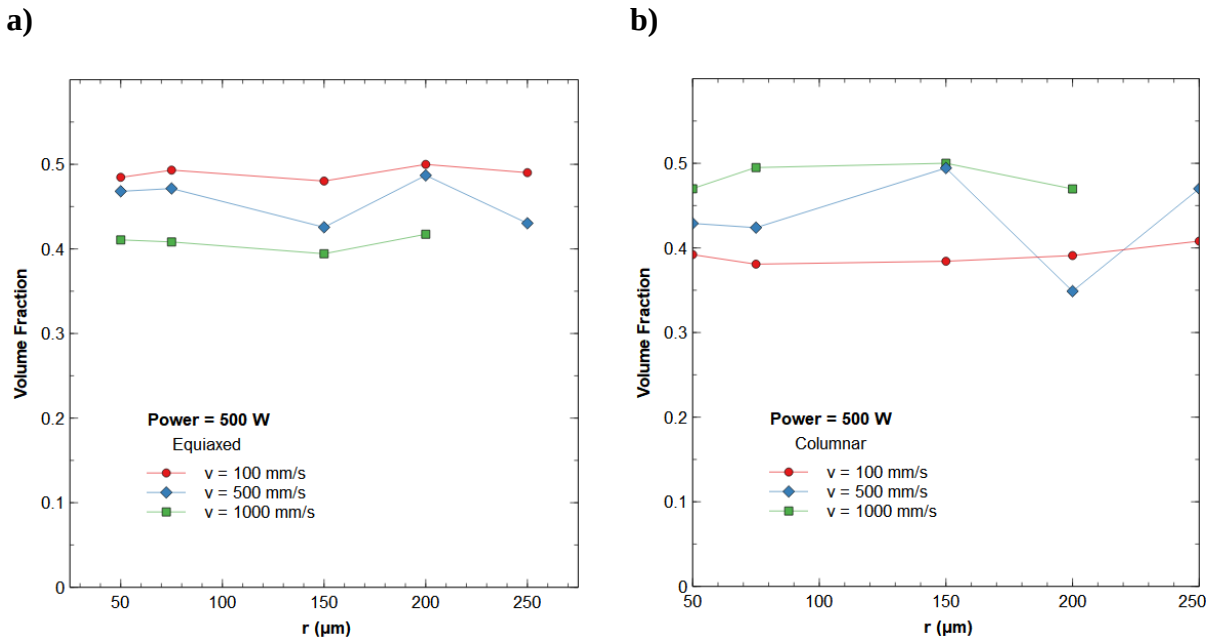

Figure 19. The volume fraction of a) equiaxed and b) columnar microstructures for circular configurations at P = 500 W.

From Figures 18a and 19a, it is generally apparent that the volume fraction of equiaxed grains decreases as laser scanning speed increases. For a *P* of 500 W at 100 mm/s, the average percentage of equiaxed microstructure is about 50%, whereas, at 1000 mm/s, the average percentage of

equiaxed microstructure is about 41%. This trend is valid for all power settings and laser scanning speeds except for *P* of 300 W at 100 mm/s. Here, at 100 mm/s, the average percentage of equiaxed growth is about 30%, whereas the average for 500 mm/s and 1000 mm/s are 39% and 34%, respectively. The overall observed trend of this work would suggest that the average volume fraction for 100 mm/s should be between 40 and 45%, although the numerical prediction shows a different trend.

An increase in laser power increases the volume fraction of equiaxed grains. The resulting average percentage of equiaxed microstructure for a *P* of 300 W at 1000 mm/s is about 34%, whereas the resulting average percentage of equiaxed microstructure for a *P* of 500 W at 1000 mm/s is about 41%. In contrast, the volume fraction of columnar microstructure increases overall as laser scanning speed increases and decreases as laser power increases.

Comparing the results of the circular simulations to those of the hexagonal simulations, it is shown that the hexagonal configuration is likely to produce a higher percentage of equiaxed microstructure. For example, for *P* of 500 at 100 mm/s, the average percentage of equiaxed grain from the hexagonal configuration is about 55%, whereas the circular configuration produces about a 49% equiaxed microstructure.

4. Conclusion

From the results obtained in this work from the simulations of synchronized hexagonal and circular arrays of lasers utilized in the LPBF application in the additive manufacturing of Ti-6Al-4V, it is possible to control the microstructure of material via laser parameters including power, scanning speed, and spacing. Generally, increasing laser power or decreasing the scanning speed increases the volume fraction of equiaxed grains. Also, increasing scanning speed decreases grain size. In

addition, larger internal spacing between laser beams increases the melt pool width and decreases the melt pool depth. Also, the large spacing at higher scanning speeds and low laser power settings can result in discontinuous melt pools and thermal gradients; therefore, it is suggested that some laser overlap at lower power settings and higher scanning speeds be utilized to ensure a continuous melt pool and promote the occurrence of equiaxed microstructure.

5. Future Work

This work's results indicate the feasibility of microstructure control via M-LPBF additive manufacturing, i.e., a 55% equiaxed microstructure is obtained via a hexagonal configuration with each laser at a moderate laser power of 500 W and scanning speed of 100 mm/s. It would be of interest to discover a practical set of conditions that could be utilized to obtain a fully equiaxed microstructure. The apparent considerations from the results of this work would be to investigate higher laser power settings or slower scanning speeds. At the risk of increased computational time and cost, one could consider alternate configurations with even more laser beams. Variable laser power settings within the same multi-laser configuration could be explored. However, the most exciting possible avenue for future exploration of this work could be its practical application.

Appendix

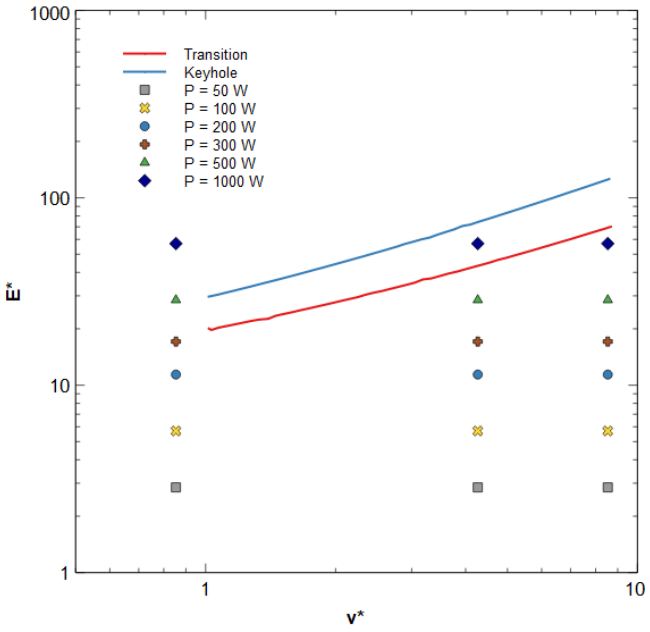

Figure 20. Processing diagram of Ti-6Al-4V for LPBF using dimensionless heat input (E) and dimensionless laser scanning speed (v*).*

Table 2. Density, thermal conductivity, and specific heat of Ti-6Al-4V [32].

Temperature (K)	Density (kg/m^3)	Thermal Conductivity (W/m·K)	Specific Heat (J/K·kg)
298	4420	7	546
373	4406	7.45	562
473	4395	8.75	584
573	4381	10.15	606
673	4366	11.35	629
773	4350	12.6	651
873	4336	14.2	673
973	4324	15.5	694
1073	4309	17.8	714
1173	4294	20.2	734
1273	4282	19.3	641
1373	4267	21	660
1473	4252	22.9	678
1573	4240	23.7	696
1673	4225	24.6	714
1773	4205	25.8	732
1873	4198	27	-

Table 3. Experimental results from single-laser configuration [22].

Speed (mm/s)	Width (μm)	Depth (μm)
500	183.1578947	79.44598338
600	147.700831	68.36565097
700	137.5069252	66.14958449
800	133.5180055	61.71745152
900	124.2105263	55.51246537
1000	120	49.75069252

Table 4. Numerical results and percent error when compared to experimental results for single-laser configuration.

Speed (mm/s)	Width (μm)	% Error in Width	Depth (μm)	% Error in Depth	Max. Temperature (K)
500	180	-1.72414	75.4	-5.09275	2459
600	165	11.7123	69.3	1.366694	2425
700	161	17.08501	60.5	-8.54062	2401
800	155	16.08921	53.2	-13.8007	2374
900	149	19.95763	50.6	-8.8493	2349
1000	142	18.33333	45.9	-7.73998	2331

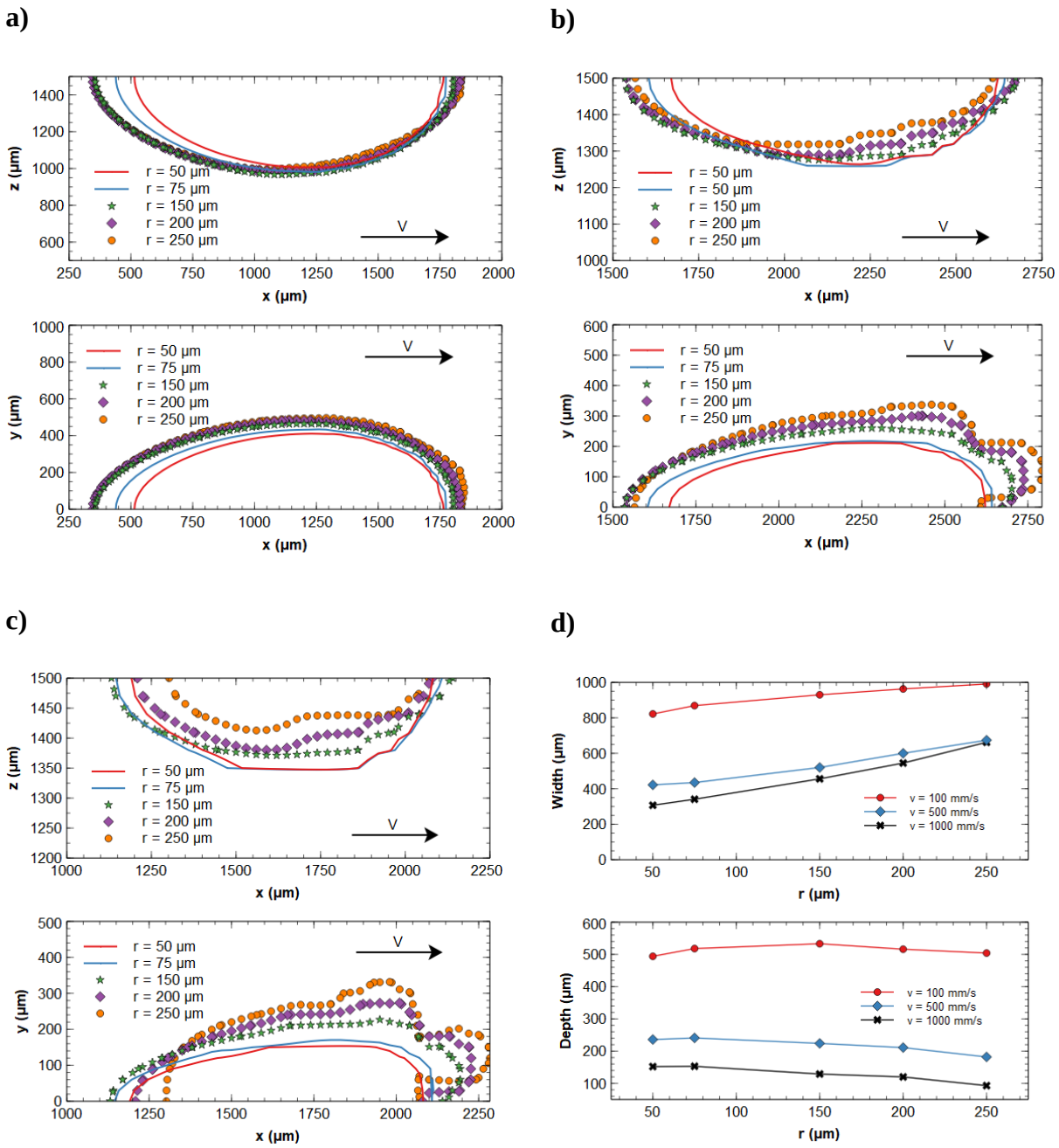

Figure 21. Melt pool shapes for all hexagonal configurations at P = 300 W for a) 100 mm/s, b) 500 mm/s, and c) 1000 mm/s and d) melt pool dimensions.

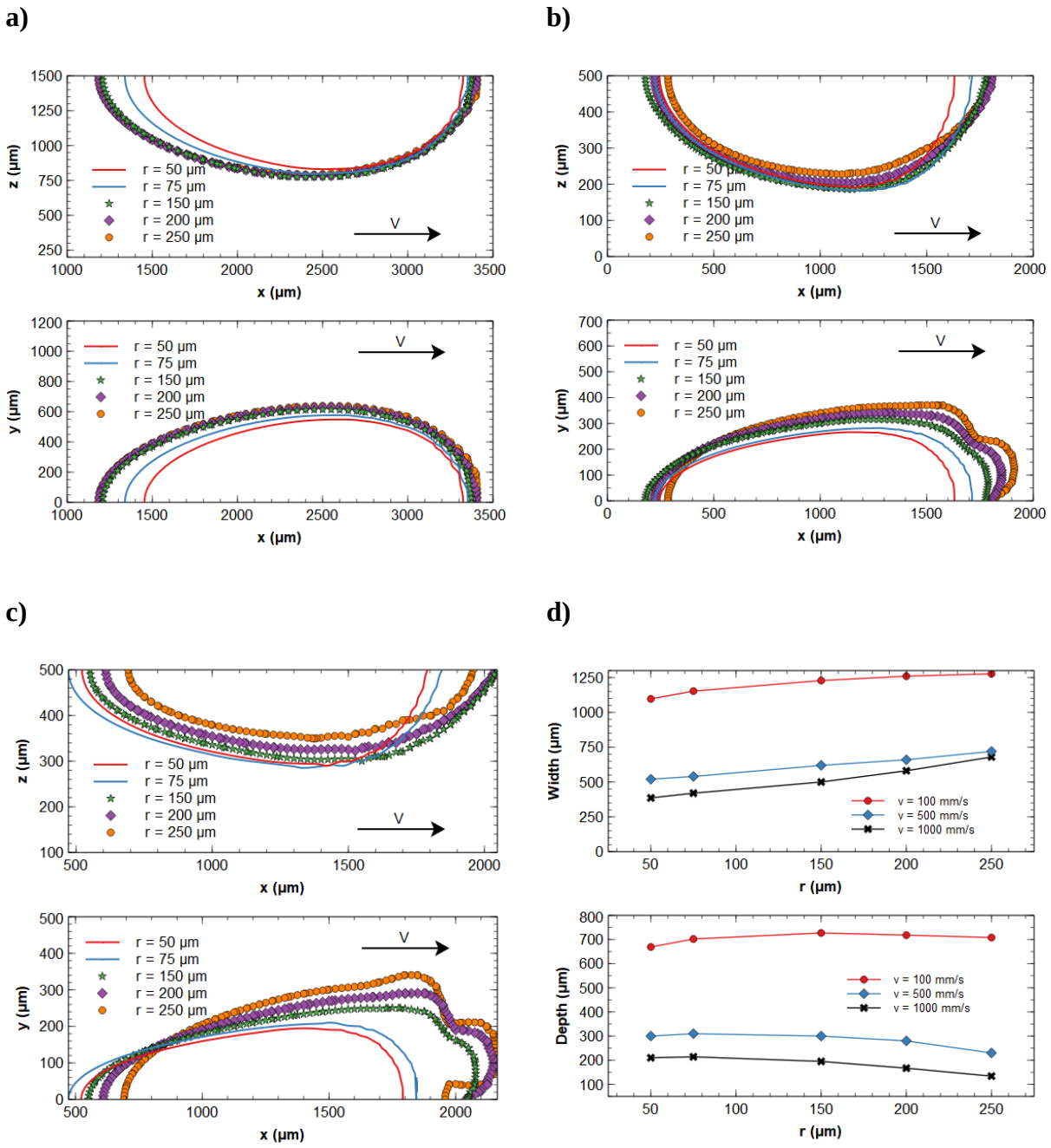

Figure 22. Melt pool shapes for all hexagonal configurations at P = 500 W for a) 100 mm/s, b) 500 mm/s, and c) 1000 mm/s and d) melt pool dimensions.

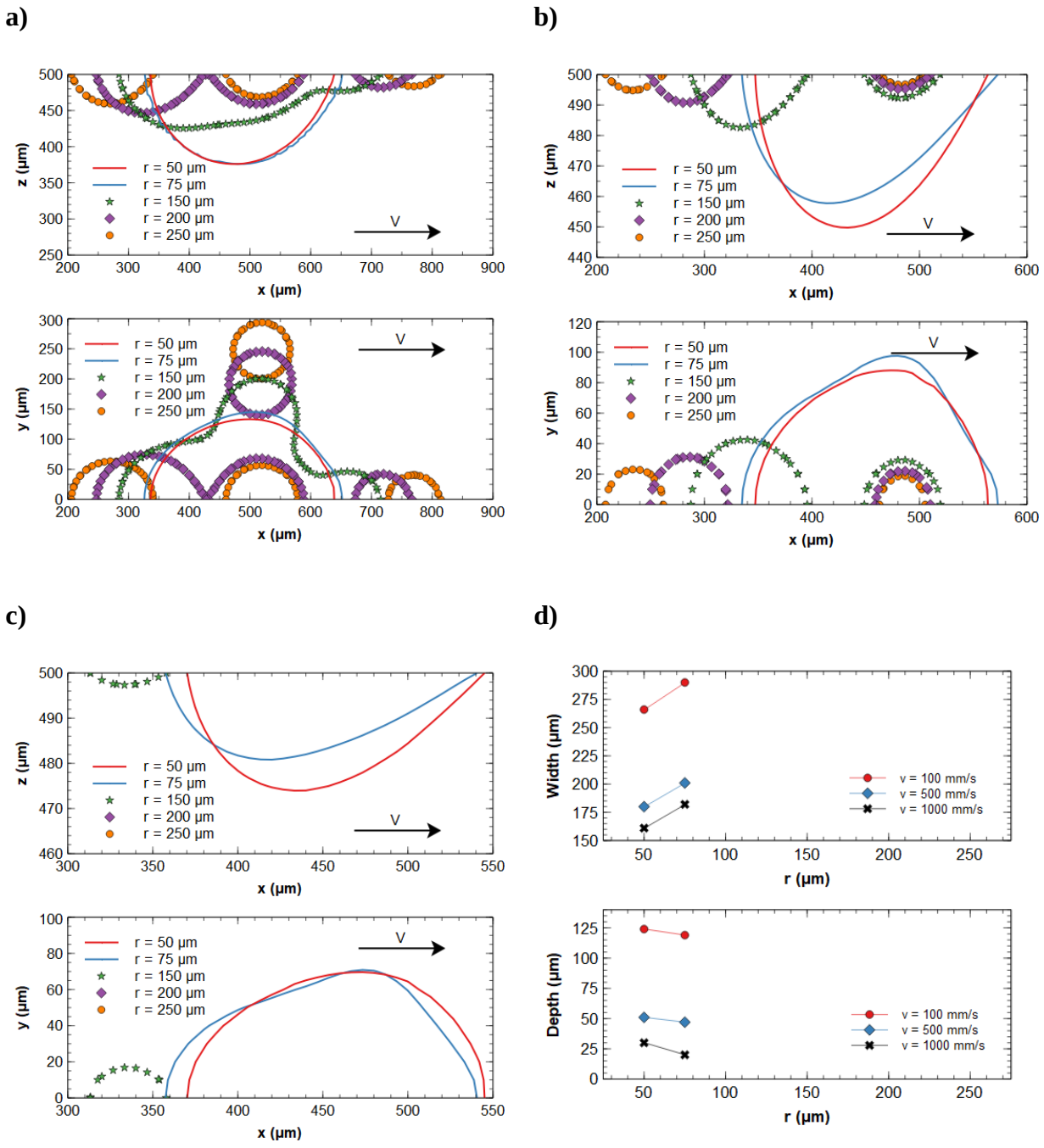

Figure 23. Melt pool shapes for all circular configurations at P = 50 W for a) 100 mm/s, b) 500 mm/s, and c) 1000 mm/s and d) melt pool dimensions.

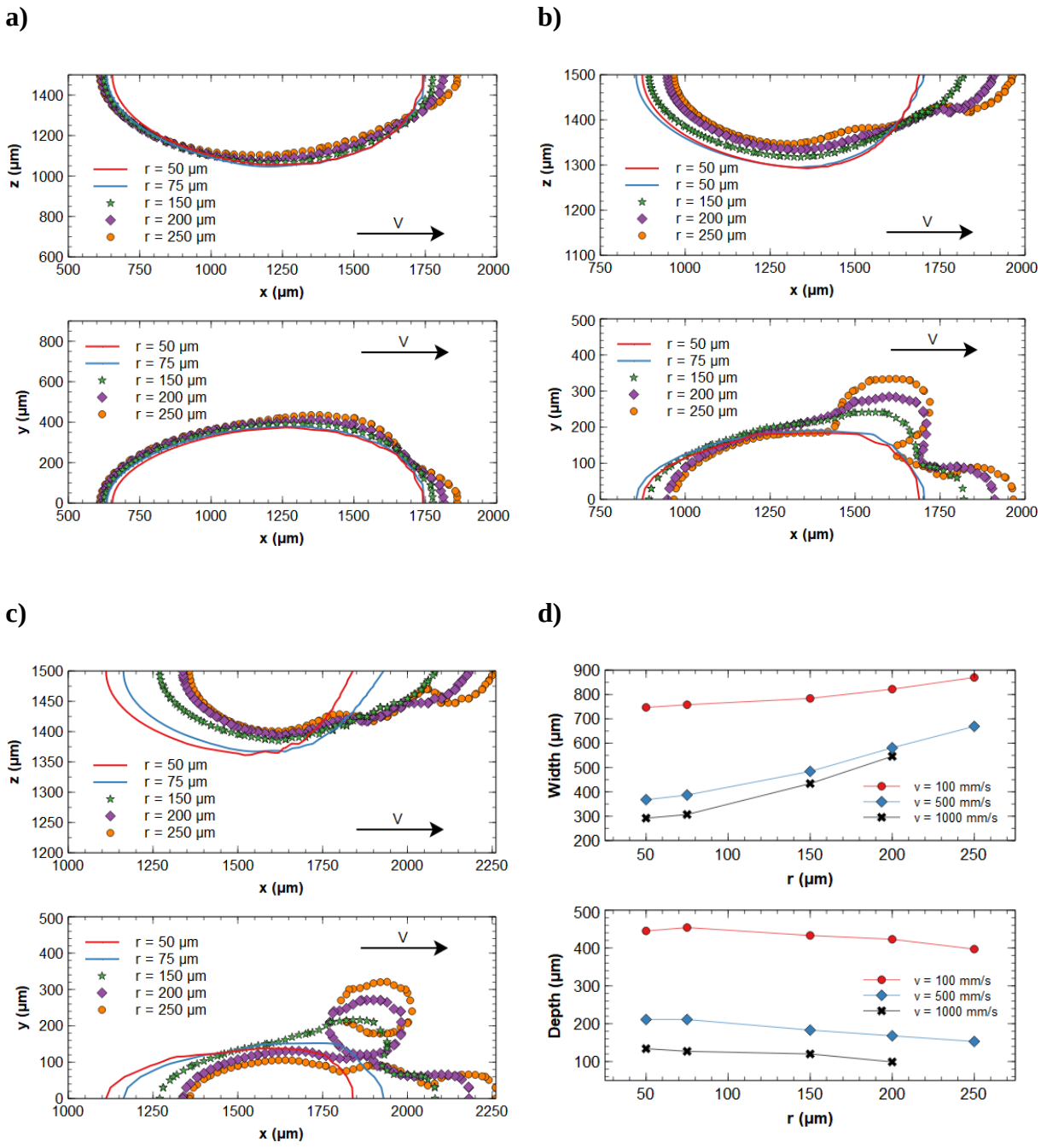

Figure 24. Melt pool shapes for all circular configurations at P = 300 W for a) 100 mm/s, b) 500 mm/s, and c) 1000 mm/s and d) melt pool dimensions.

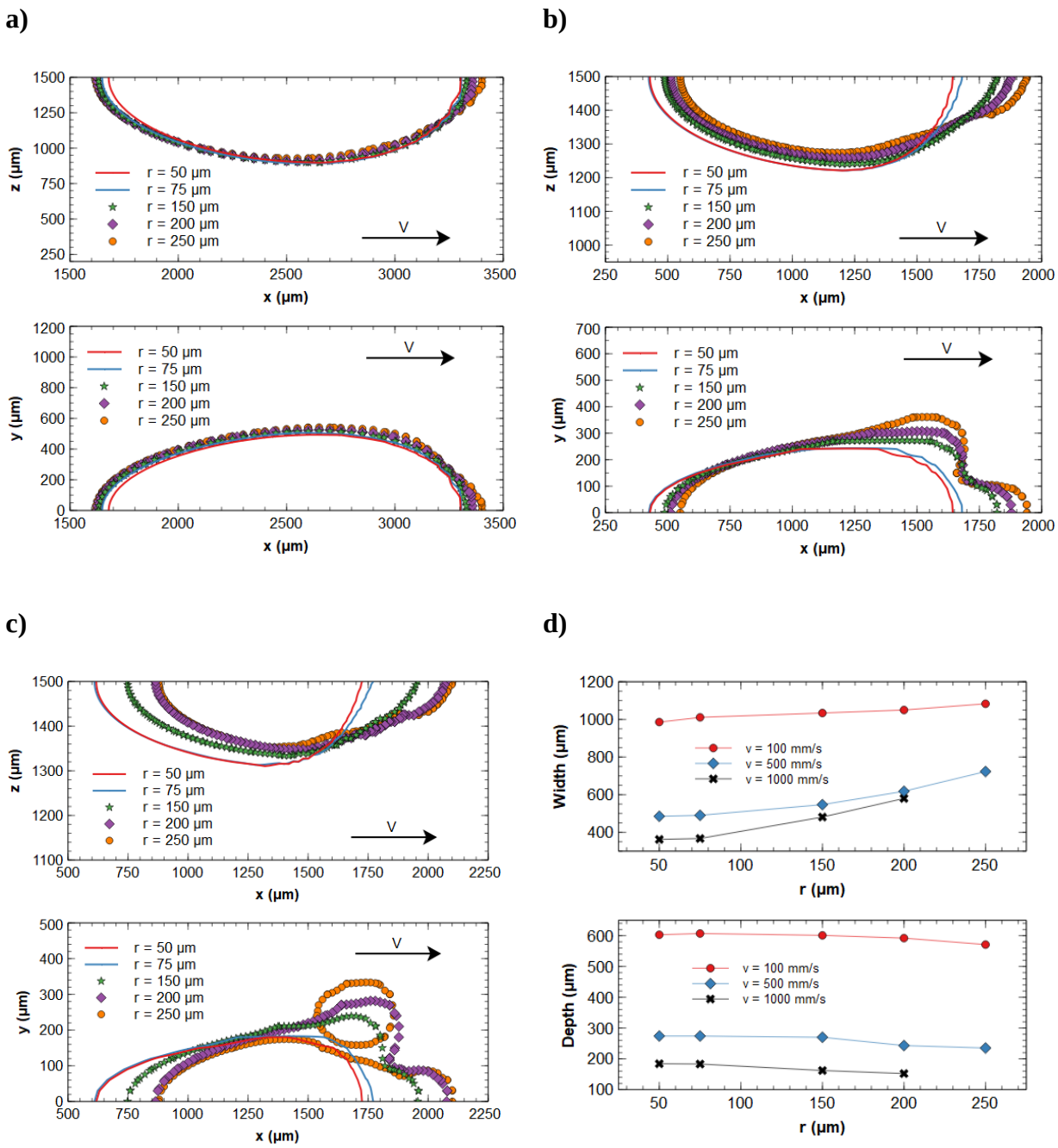

Figure 25. Melt pool shapes for all circular configurations at P = 500 W for a) 100 mm/s, b) 500 mm/s, and c) 1000 mm/s and d) melt pool dimensions.

References

[1] E. MacDonald, R. Wicker, Multiprocess 3D printing for increasing component functionality, Science. 353 (2016). https://doi.org/10.1126/SCIENCE.AAF2093.

[2] C.L.A. Leung, S. Marussi, R.C. Atwood, M. Towrie, P.J. Withers, P.D. Lee, In situ X-ray imaging of defect and molten pool dynamics in laser additive manufacturing, Nature Communications 2018 9:1. 9 (2018) 1–9. https://doi.org/10.1038/s41467-018-03734-7.

[3] A. du Plessis, I. Yadroitsava, I. Yadroitsev. Effects of defects on mechanical properties in metal additive manufacturing: A review focusing on X-ray tomography insights, Materials and Design. Vol. 185, 2020. https://doi.org/10.1016/j.matdes.2019.108385

[4] X. Wu, J. Liang, J. Mei, C. Mitchell, P.S. Goodwin, W. Voice, Microstructures of laserdeposited Ti–6Al–4V, Materials & Design. 25 (2004) 137–144. https://doi.org/10.1016/J.MATDES.2003.09.009.

[5] J. Li, X. Zhou, M. Brochu, N. Provatas, Y.F. Zhao. Solidification microstructure simulation of Ti-6Al-4V in metal additive manufacturing: A review, Additive Manufacturing. 31 (2020). https://doi.org/10.1016/j.addma.2019.100989

[6] S. Gorsse, C. Hutchinson, M. Gouné, R. Banerjee. Additive manufacturing of metals: a brief review of the characteristic microstructures and properties of steels, Ti-6Al-4V and high-entropy alloys, Science and Technology of Advanced Materials, 18 (2017) 584–610. doi: 10.1080/14686996.2017.1361305

[7] R. Evans, J. Gockel, Modeling the effects of coordinated multi-beam additive manufacturing, The International Journal of Advanced Manufacturing Technology 2021 115:4. 115 (2021) 1075–1087. https://doi.org/10.1007/S00170-021-07279-W.

[8] A.R.A. Dezfoli, W.-S. Hwang, W.-C. Huang, T.-W. Tsai, Determination and controlling of grain structure of metals after laser incidence: Theoretical approach, Scientific Reports 2017 7:1. 7 (2017) 1–11. https://doi.org/10.1038/srep41527.

[9] T. Heeling, K. Wegener, The effect of multi-beam strategies on selective laser melting of stainless steel 316L, Additive Manufacturing. 22 (2018) 334–342. https://doi.org/10.1016/J.ADDMA.2018.05.026.

[10] G. Lewandowski, Engineering of Temperature Profiles for Location-Specific Control of Material Micro-Structure in Laser Powder Bed Fusion Additive Manufacturing, (2020).

[11] T. Heeling, K. Wegener, Computational Investigation of Synchronized Multibeam Strategies for the Selective Laser Melting Process, Physics Procedia. 83 (2016) 899–908. https://doi.org/10.1016/J.PHPRO.2016.08.094.

[12] P. Promoppatum, S.C. Yao, P.C. Pistorius, A.D. Rollett, A Comprehensive Comparison of the Analytical and Numerical Prediction of the Thermal History and Solidification Microstructure of Inconel 718 Products Made by Laser Powder-Bed Fusion, Engineering. 3 (2017) 685–694. https://doi.org/10.1016/J.ENG.2017.05.023.

[13] Localized Preheating Approaches for Reducing Residual Stress in Additive Manufacturing n.d. https://repositories.lib.utexas.edu/handle/2152/80153 (accessed January 20, 2021).

[14] J. Wilkes, Y.C. Hagedorn, W. Meiners, K. Wissenbach, Additive manufacturing of ZrO2- Al2O3 ceramic components by selective laser melting, Rapid Prototyping Journal. 19 (2013) 51–57. https://doi.org/10.1108/13552541311292736.

[15] F. Abe, K. Osakada, M. Shiomi, K. Uematsu, M. Matsumoto, The manufacturing of hard tools from metallic powders by selective laser melting, Journal of Materials Processing Technology. 111 (2001) 210–213. https://doi.org/10.1016/S0924-0136(01)00522-2.

[16] W. Zhang, M. Tong, N.M. Harrison, Scanning strategies effect on temperature, residual stress and deformation by multi-laser beam powder bed fusion manufacturing, Additive Manufacturing. 36 (2020) 101507. https://doi.org/10.1016/J.ADDMA.2020.101507.

[17] M. Gerstgrasser, M. Cloots, J. Stirnimann, K. Wegener, Residual stress reduction of LPBFprocessed CM247LC samples via multi laser beam strategies, The International Journal of Advanced Manufacturing Technology 2021. (2021) 1–11. https://doi.org/10.1007/S00170- 021-07083-6.

[18] J. Yin, D. Wang, H. Wei, L. Yang, L. Ke, M. Hu, W. Xiong, G. Wang, H. Zhu, X. Zeng, Dual-beam laser-matter interaction at overlap region during multi-laser powder bed fusion manufacturing, Additive Manufacturing. 46 (2021) 102178. https://doi.org/10.1016/J.ADDMA.2021.102178.

[19] J. Ye, S.A. Khairallah, A.M. Rubenchik, M.F. Crumb, G. Guss, J. Belak, M.J. Matthews, Energy Coupling Mechanisms and Scaling Behavior Associated with Laser

Powder Bed Fusion Additive Manufacturing, Advanced Engineering Materials. 21 (2019) 1900185. https://doi.org/10.1002/ADEM.201900185.

[20] S. Patel, M. Vlasea, Melting modes in laser powder bed fusion, Materialia. 9 (2020) 100591. https://doi.org/10.1016/J.MTLA.2020.100591.

[21] TOULOUKIAN, Y. S., Thermal conductivity, Nonmetallic Solids, Thermophys. Properties of Matter. 2 (1970) 183–193. https://ci.nii.ac.jp/naid/10005748060 (accessed January 21, 2021).

[22] J. Yin, G. Peng, C. Chen, J. Yang, H. Zhu, L. Ke, Z. Wang, D. Wang, M. Ma, G. Wang, X. Zeng, Thermal behavior and grain growth orientation during selective laser melting of Ti6Al-4V alloy, Journal of Materials Processing Technology. 260 (2018) 57–65. https://doi.org/10.1016/J.JMATPROTEC.2018.04.035.

[23] Z. Zhang, Y. Huang, A. Rani Kasinathan, S. Imani Shahabad, U. Ali, Y. Mahmoodkhani, E. Toyserkani, 3-Dimensional heat transfer modeling for laser powder-bed fusion additive manufacturing with volumetric heat sources based on varied thermal conductivity and absorptivity, Optics & Laser Technology. 109 (2019) 297–312. https://doi.org/10.1016/J.OPTLASTEC.2018.08.012.

[24] Yang J, Sun S, Brandt M, Yan W. Experimental investigation and 3D finite element prediction of the heat affected zone during laser assisted machining of Ti6Al4V alloy. Journal of Materials Processing Technology 2010;210:2215–22. https://doi.org/10.1016/J.JMATPROTEC.2010.08.007.

[25] AK Unni, M. Vasudevan, Determination of heat source model for simulating full penetration laser welding of 316 LN stainless steel by computational fluid dynamics,

Materials Today: Proceedings. 45 (2021) 4465–4471. https://doi.org/10.1016/J.MATPR.2020.12.842.

[26] I.A. Roberts, C.J. Wang, R. Esterlein, M. Stanford, D.J. Mynors, A three-dimensional finite element analysis of the temperature field during laser melting of metal powders in additive layer manufacturing, International Journal of Machine Tools and Manufacture. 49 (2009) 916–923. https://doi.org/10.1016/J.IJMACHTOOLS.2009.07.004.

[27] Z. Zhang, Y. Huang, A. Rani Kasinathan, S. Imani Shahabad, U. Ali, Y. Mahmoodkhani, E. Toyserkani, 3-Dimensional heat transfer modeling for laser powder-bed fusion additive manufacturing with volumetric heat sources based on varied thermal conductivity and absorptivity, Optics & Laser Technology. 109 (2019) 297–312. https://doi.org/10.1016/J.OPTLASTEC.2018.08.012.

[28] Q. Chen, G. Guillemot, C.A. Gandin, M. Bellet, Numerical modelling of the impact of energy distribution and Marangoni surface tension on track shape in selective laser melting of ceramic material, Additive Manufacturing. 21 (2018) 713–723. https://doi.org/10.1016/J.ADDMA.2018.03.003.

[29] S. Bontha, N.W. Klingbeil, P.A. Kobryn, H.L. Fraser, Effects of process variables and sizescale on solidification microstructure in beam-based fabrication of bulky 3D structures, Materials Science and Engineering: A. 513–514 (2009) 311–318. https://doi.org/10.1016/J.MSEA.2009.02.019.

[30] PA Kobryn, S.L. Semiatin, Microstructure and texture evolution during solidification processing of Ti–6Al–4V, Journal of Materials Processing Technology. 135 (2003) 330– 339. https://doi.org/10.1016/S0924-0136(02)00865-8.

[31] Y. He, M. Zhong, N. Jones, J. Beuth, B. Webler, The Columnar-to-Equiaxed Transition in Melt Pools During Laser Powder Bed Fusion of M2 Steel, Metallurgical and Materials Transactions A: Physical Metallurgy and Materials Science. 52 (2021) 4206–4221. https://doi.org/10.1007/S11661-021-06380-9/FIGURES/11.

[32] K.C. Mills, Recommended values of thermophysical properties for selected commercial alloys, Woodhead Publishing, 2002.